

CHARACTERIZATION OF LASER DIRECT DEPOSITED MAGNESIUM ALUMINATE SPINEL CERAMICS

John M. Pappas, Xiangyang Dong*

Department of Mechanical and Aerospace Engineering, Missouri University of Science and
Technology, Rolla, MO 65409.

Abstract

An additive manufacturing (AM) approach, via laser direct deposition, is investigated in printing transparent magnesium aluminate spinel (MAS) ceramics. Using AM, traditionally difficult or expensive to manufacture shapes, such as optical lenses, can be rapidly manufactured to near net shape, reducing time consuming and expensive post processing requirements. The transparency of MAS ceramics is highly dependent on the microstructure, with porosity and microcracking having the largest effect on the transparency of fabricated parts. With high localized heat inherent in the laser deposition process, the microstructure of ceramic parts can be controlled by adjusting processing parameters. In this study, thin wall MAS structures were fabricated by varying processing parameters. Processing parameters including laser scan speed and laser power had a large influence on the part quality. To fabricate transparent magnesium aluminate spinel ceramics with high mechanical properties, the effects of processing parameters on part porosity, density, and microstructure were studied. Dense MAS parts were successfully fabricated through the laser direct deposition process. Low scan speed and high laser power showed the most promising results in fabricating MAS parts of low porosity. Using a low powder flow rates of 0.58 g/min, a relative density of nearly 98% was achieved. Directional cooling through the substrate and from the powder conveying gas led to columnar grain growth at a tilt angle from the build direction. The primary defects of fabricated MAS ceramics were found to be residual porosity and microcracking, which negatively affected part transparency and mechanical properties. Typical microcracking patterns included transverse and longitudinal cracking, with longitudinal cracks being more prevalent due to the existence of columnar grains and intergranular fracture mode. A preliminary study demonstrated that a certain degree of transparency was achieved in additively manufactured MAS ceramic parts via laser direct deposition.

Keywords: Transparent ceramics, Magnesium aluminate spinel, Laser direct deposition, Additive manufacturing

Introduction

Transparent ceramics have many useful applications including transparent armor, lenses, and other optical elements. Among them, magnesium aluminate spinel (MAS) ceramics are of particular interest due to high in-line transmittance [1] and the highest hardness compared to other transparent materials [2], along with other desirable properties including cubic crystalline structure, which is optically isotropic and has high transmission values through a wide variety of grain sizes [3]. Non-cubic polycrystalline ceramics, such as α -alumina, are much more difficult to manufacture with high transparency due to birefringent nature, where light is scattered by grain

* Corresponding Author: dongxi@mst.edu, 1-573-341-4373 (ph), 1-573-341-4607 (fax)

boundaries [4], and non-cubic polycrystalline ceramics must have sub-micrometer grain size to be transparent [5]. In particular, considering the challenges still encountered in controlling grain size and orientation via additive manufacturing (AM) [6], cubic polycrystalline ceramics, including MAS, work as a better alternative in fabrication of transparent parts over non-cubic polycrystalline ceramics for the laser direct deposition process described in this paper.

Previous studies showed that a major challenge of laser deposition-based AM was the difficulty in fabricating fully dense parts due to residual porosity. Porosity negatively affects the optical properties of transparent ceramics through radiation scattering mechanisms [5-6]. Residual porosity is the main cause of reduced transparency of fabricated parts, especially in the visible and ultraviolet range [9]. Depending on the number of pores and void size, fabricated parts can either exhibit opaque or translucent characteristics instead of true transparency. If pore size is close to the optical wavelength, transmittance through the ceramic is at a minimum, with small pores showing much less optical scattering than larger pores [10]. To be transparent, materials must have a residual porosity of <0.1% with pore sizes less than 100nm [1]. To have very high-glass like transmittance, residual porosity must be further reduced to <0.01% [11]. Porosity formation is highly process dependent; by adjusting processing parameters, the prevalence and size of pores can be affected to a large extent. Mahamood et al. [12] found that laser power and scan speed played significant roles in residual porosity. It was shown that with increased laser power, and decreased scan speed, porosity was reduced. Porosity-free Ti6Al4V parts could be obtained at a laser power of 800 W and a scan speed of 5 mm/min fabricated by laser metal deposition. Ning et al. [13] found that using an ultrasonic vibration table, porosity was significantly reduced for Inconel 718 parts fabricated with the laser engineered net shaping process. This was attributed to the acoustic streaming and cavitation effect caused by ultrasonic vibrations.

In addition to porosity, microstructural characterization and control of resultant microcracking, grain size, and grain distribution are very important due to the potential impacts they have on transparency and mechanical properties of fabricated parts. Cracks severely weaken the mechanical properties and negatively affect the transparency of parts. Therefore, research work has been done to minimize or eliminate process-induced cracks as much as possible. Niu et al. [14] found that crack formation and prevalence was significantly affected by layer thickness for pure alumina structures fabricated with laser engineered net shaping. In this study, it was found that crack prevalence significantly decreased with increasing layer thickness, and at layer thickness of 0.8 mm and above, nearly crack-free specimens were produced. In a related study, Niu et al. [15] found that increasing laser scan speed decreased the number of cracks in pure alumina ceramics produced by laser engineered net shaping, and a scan speeds greater than 700 mm/min produced crack-free structures. This result was attributed to increased scan speed decreasing thermal stress and increasing fracture strength. Inclusion of ultrasonic-vibration during laser engineered net shaping of alumina-zirconia parts was studied by Hu et al. [16]. It was found that crack initiation and propagation were suppressed due to the addition of ultrasonic vibration, which was primarily attributed to grain refinement and reduced thermal stress. Additional benefits of using ultrasonic vibration during fabrication were increased mechanical properties including microhardness, wear resistance, and compressive strength. Balla et al. [17] found that alumina ceramics fabricated with laser engineered net shaping showed anisotropic mechanical properties due to columnar grain solidification along the build direction, with marginal increases in strength after additional high-heat treatment. Niu et al [18] found that columnar grains in pure alumina ceramics produced by

laser engineered net shaping are typically larger in ceramics produced by sintering methods, and metals prepared with the same method. It was proposed that a primary reason for this was due to the low thermal conductivity of ceramics causing heat accumulation during fabrication.

With a focus on transparent ceramics, the goal of this work is to study the effects of processing parameters and powder precursors on part residual porosity and microstructure as well as investigate the viability of laser direct deposition for MAS. Due to the critical role that porosity plays in transparency of these ceramics, the effect of processing conditions on resultant porosity was a key focus in this paper. While there has been considerable work on AM of non-transparent ceramics via selective laser melting (SLM) [19]–[22] and laser engineered net shaping [16], [18], [23], [24], there is a lack of work on transparent ceramics, including MAS. This could be attributed to difficulties in additively manufacturing MAS ceramics due to process related porosity and cracking. Therefore, it is necessary to characterize the microstructure of direct laser deposited MAS ceramics and determine which processing conditions mostly affect residual porosity on the fabricated parts.

Experimental Procedure

2.1 Powder Preparation

The materials in this study included MgO powders purchased from Sigma-Aldrich (Part No. 342793) with a purity greater than 99% and average particle sizes less than 44 μm . The MgO powders were used with Al_2O_3 powder from Almatix (A3500 UG) with a purity of greater than 99.5% and D-50 particle size of about 2.2 μm . An excellent flowability was observed for the selected powders during the fabrication processes in this study. Following the stoichiometric ratio of MAS, the powder was first mixed in a ball mill for two hours using alumina grinding media and acetone solvent. Acetone solvent was removed with a Buchi R124 rotary evaporator. Following the rotary evaporation, the powder was calcined with forced air flow for eight hours in a Lindberg furnace at 600 $^\circ\text{C}$ to burn out any organic contamination, especially residual acetone and dehydrate the MgO powder.

It is worth noting that in this study, the MAS ceramics were directly synthesized from the Al_2O_3 -MgO powder mixtures via melt-grown methods during laser direct deposition. This method of synthesis was chosen due to the difficulties in purchasing commercially available MAS powders that showed consistent and repeatable flowability required in the powder feeding process for laser deposition in this study. Therefore, alumina and magnesia powders that showed good flowability were first chosen and mixed as described previously. Due to low availability of spinel powders, options are very limited with respect to particle shape and size, both of which significantly influence how powders will flow in the powder feeding processes. Preliminary studies were performed using the MAS powder from Sigma-Aldrich with an average particle size of < 50 nm. Testing with this powder proved the difficulty of maintaining a consistent powder flow, which resulted in very poor deposition quality, as depicted in Figure 1. In addition to the improved flowability needed in powder feeding processes, the synthesis method used in this study showed greater potentials in reducing the manufacturing costs, considering the availability of magnesia and alumina powders separately. In contrast, commercially available spinel powders are

commonly more expensive and difficult to obtain at the specific stoichiometric composition for MAS.

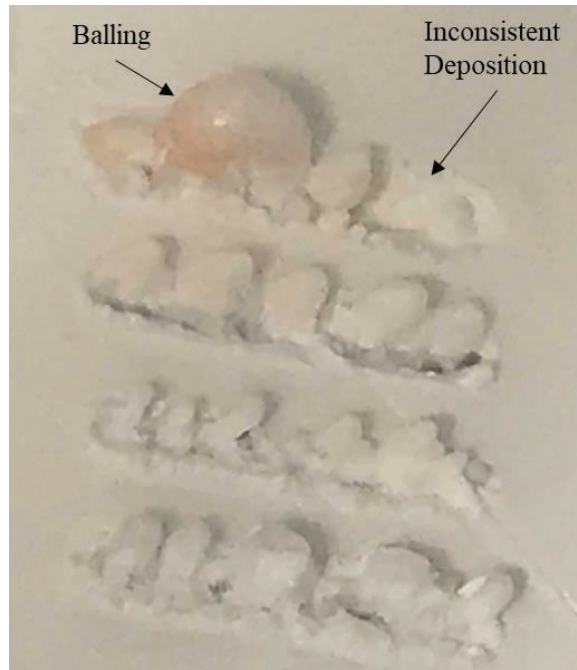


Figure 1: Image showing poor deposition quality of commercially available MAS powders due to inconsistent powder flow, which illustrates the main benefit of the laser-melting method of spinel synthesis from magnesia and alumina powder mixtures.

It has also been observed that a potential issue with this synthesis process was related to MgO, which is a hygroscopic substance and readily reacts with water vapor in the air to form magnesium hydroxide ($\text{Mg}(\text{OH})_2$). If the powder was exposed to moisture before processing, the flowability of the powder was seen to be severely limited, making it difficult to accurately control the powder flow rate. Hydrated powder may introduce additional gasses into laser processing, thus increasing residual porosity in fabricated parts. Decomposition of $\text{Mg}(\text{OH})_2$ occurs at temperatures greater than $450\text{ }^\circ\text{C}$ [27], [28], thus requiring calcination immediately prior laser deposition. This necessitates the need of careful preparation of $\text{Al}_2\text{O}_3\text{-MgO}$ powder mixtures with a burn-out procedure added in this study.

2.2 Experimental Setup and Characterization

CoorsTek AD-998 alumina substrates with 99.8% purity were used in this study for thermal expansion compatibility with deposited MAS. The laser direct deposition setup used in this study is shown in Figure 2 and includes a Convergent Energy Arrow Ultimate CO_2 laser with maximum continuous wave (CW) output of 1.7 kW at $10.6\text{ }\mu\text{m}$ wavelength. The alumina substrate was mounted onto a 3-axis motorized table for positioning and movement. Powder delivery was controlled with a Powder Motion Labs X2W powder feeder and controller exhibiting a feed rate repeatability of less than 1%. Argon inert gas was used to feed the prepared powder mixture at a flow rate of 3 L/min. A 1.6 mm inner diameter alumina tube was used to guide the powder into the melt pool parallel to the scan direction and at an angle from the substrate.

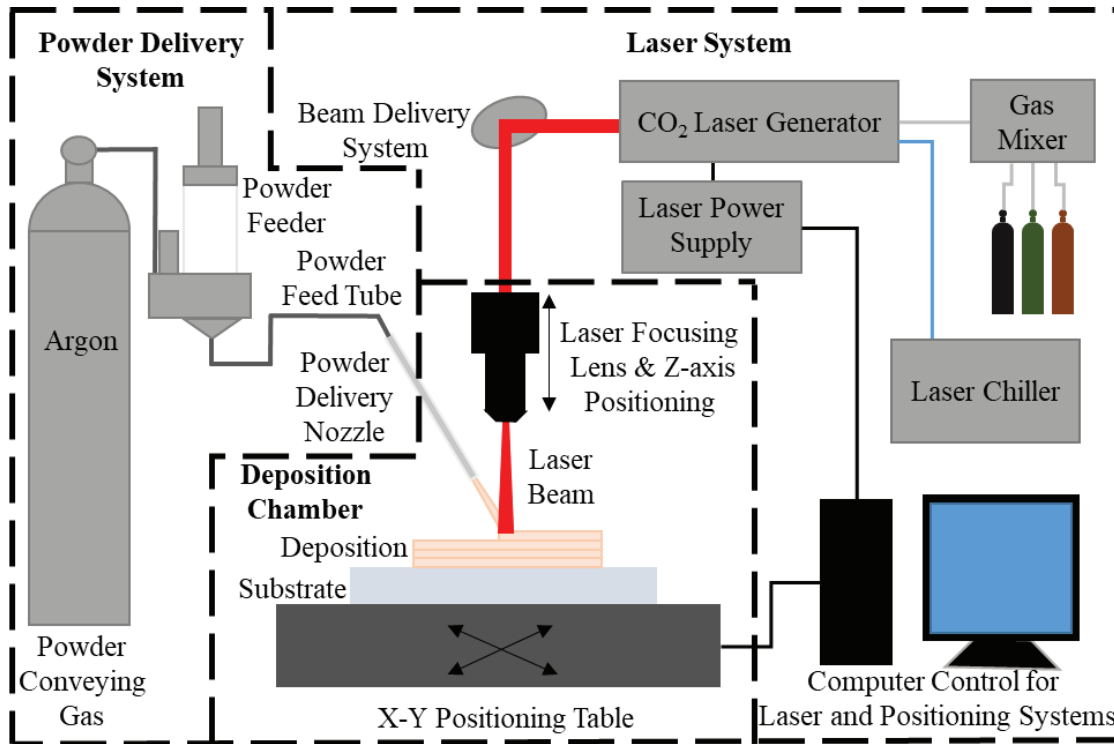


Figure 2: A schematic diagram of the experimental setup for laser direct deposition

The processing parameters used for this study are summarized in Table 1. Laser spot size was maintained at a constant diameter of 2.5 mm in this study. Parametric studies were performed by varying laser power and scan speed to study their effects on the printed ceramic parts. Thin-wall structures were built using a reciprocal scanning motion. After each track, the laser head would increment in the z-direction by Δz , which was equivalent to the layer thickness.

Table 1: Process parameters used in this study

Laser Power (W)	275, 485
Laser Spot Size (mm)	2.5
Scan Speed (mm/minute)	1000, 2000, 3000, 4000, 5000

The printed thin wall samples were then sectioned and polished for microstructural characterization. The images of the polished samples were captured using a Hirox KH-8700 digital microscope. Due to limitations in the field of view of the optical microscope, image stitching was performed in Fiji software using an image stitching plugin [29]. Due to the variations in processing conditions for the top and bottom layers, the middle sectioned were analyzed to obtain the typical microstructural characteristics. ImageJ software was used to analyze the porosity area of the fabricated MAS samples, and Archimedes' method was used for the density analysis of as-fabricated thin wall structures. To reveal the typical grain size and distribution, the polished structures were thermally etched in accordance with the guidelines in the ASM Handbook Volume 9 [30], at 1400 °C for 10 minutes.

Results and Discussion

3.1 Microstructure Characteristics of MAS Samples

Figure 3 shows the typical microstructure characteristics observed in the printed MAS samples after thermal etching. Columnar grains were primarily observed for MAS samples fabricated by laser direct deposition. Figure 3B shows the cross-sectional view of the whole sample and highlights areas taken for closer microstructural examination. Figure 3A shows the microstructure of a region deposited near the substrate. Initially deposited layers exhibited columnar grains grown at a tilt angle of approximately 20 degrees from the build direction. This was mainly due to the solidification principal of columnar grain growth occurring in the orientation of thermal gradients, opposite to the direction of heat flow, where rapid cooling rates are present [17]. The 20-degree grain orientation with respect to the build direction was attributed to the primary cooling mechanism being conducted through the substrate, with lesser convective cooling rates by the argon powder conveying gas. Hence, the largest thermal gradient for initially deposited layers was along the build direction, resulting in the observed columnar grains.

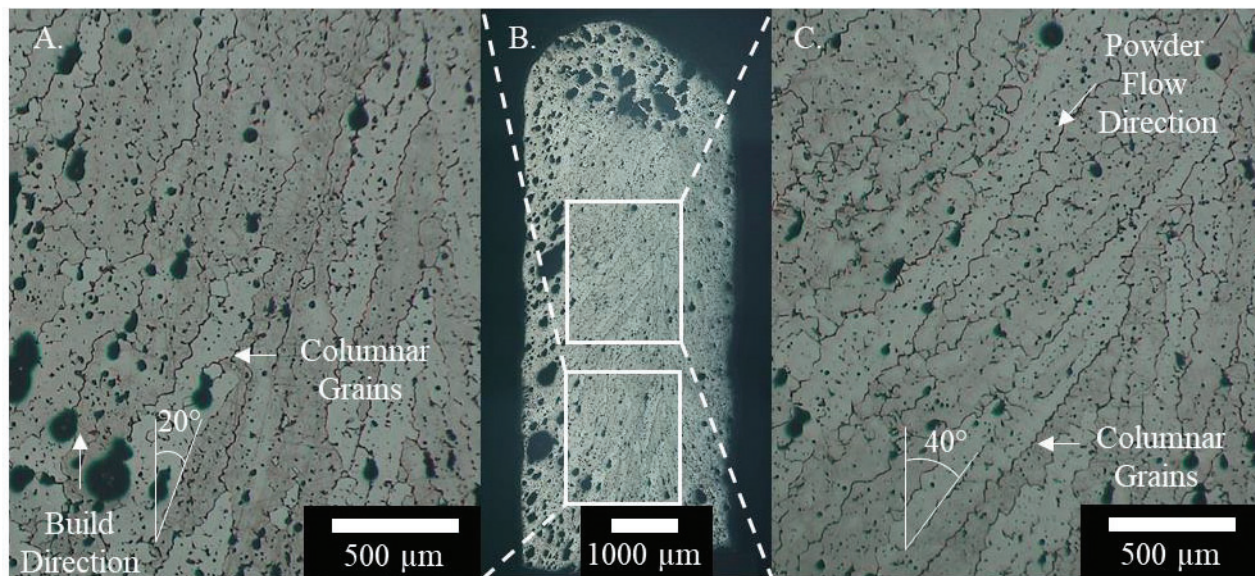


Figure 3: Typical microstructure of thin wall sample fabricated at 275 W laser power, 2000 mm/min scan speed, and 2.1 g/min powder flow rate by laser direct deposition showing: A. Columnar grains grown at a small angle from the build direction for the layers deposited near the substrate; B. Cross-sectional view of the entire sample; C. Columnar grains grown at a larger angle from the build direction for the layers deposited further from the substrate

Figure 4 depicts the side view of thin wall structures and illustrates the effects of the conveying gas plume around the thin wall structure on the side adjacent to the powder feed nozzle. The powder feed nozzle was aimed at the melt pool perpendicular to the scan direction, and at an angle from the build direction in this study. This causes a continuous flow of cool argon gas around the outer surface of the deposited structure on the right side, thus producing relatively high cooling rates, and hence thermal gradients, on one side. The opposite side was mostly blocked from the

argon flow by the structure itself and therefore experienced much lower cooling rates, which are sufficient to significantly affect grain growth.

It is also interesting to note that the layers deposited further from the substrate had an increased tilt angle of approximately 40 degrees from the build direction as shown in Figure 3C. Since the MAS ceramics were a good type of insulator materials, heat flow to the substrate reduced considerably at an elevated distance from the substrate. Therefore, the percentage of total heat loss to the side of the structure, due to convection from the powder conveying gas, increased. With this increase in transverse heat flow, grain orientation shift away from the build direction increasingly with an increased distance from the substrate.

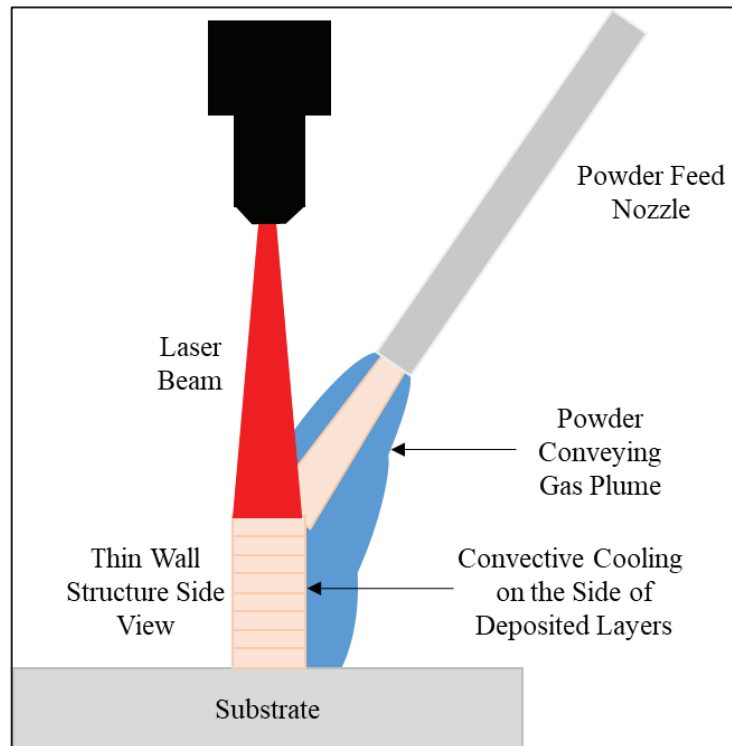


Figure 4: Schematics depicting convective cooling due to the powder conveying gas plume on one side of thin wall structures during fabrication

3.2 Cracking Characterization of MAS Samples

The primary microcrack propagation directions for MAS thin wall structures are in the build direction (longitudinal cracks) and along the scan direction (transverse cracks). Figure 5 shows a backlit sample to highlight typical cracks observed. Very high cooling rates due to laser melting and solidification processes, of up to 10^5 K/s [17], create large thermal gradients and thermal stresses in the deposited materials. The relatively high hardness of the deposited MAS ceramic material makes it very susceptible to brittle fracture, which occurs when the tensile stresses are higher than the mechanical strength [31].

It was observed that longitudinal cracks are more prevalent, and typically extended further than transverse cracks. It could be attributed to the columnar grains extended primarily along the longitudinal (build) direction. As higher fracture energy was often required for transgranular fracture, intergranular cracking would be more common in the brittle materials and thus primarily propagated along the grain boundaries of vertically elongated columnar grains [14]. On the other hand, the cooling and solidification processes of recently deposited layers led volume contraction, which was constrained by the previously solidified but cooler layers [15], thus yielding tensile stresses in the newly deposited layer. The tensile stresses initiated microcracks, which preferentially propagated along the grain boundaries as discussed above.

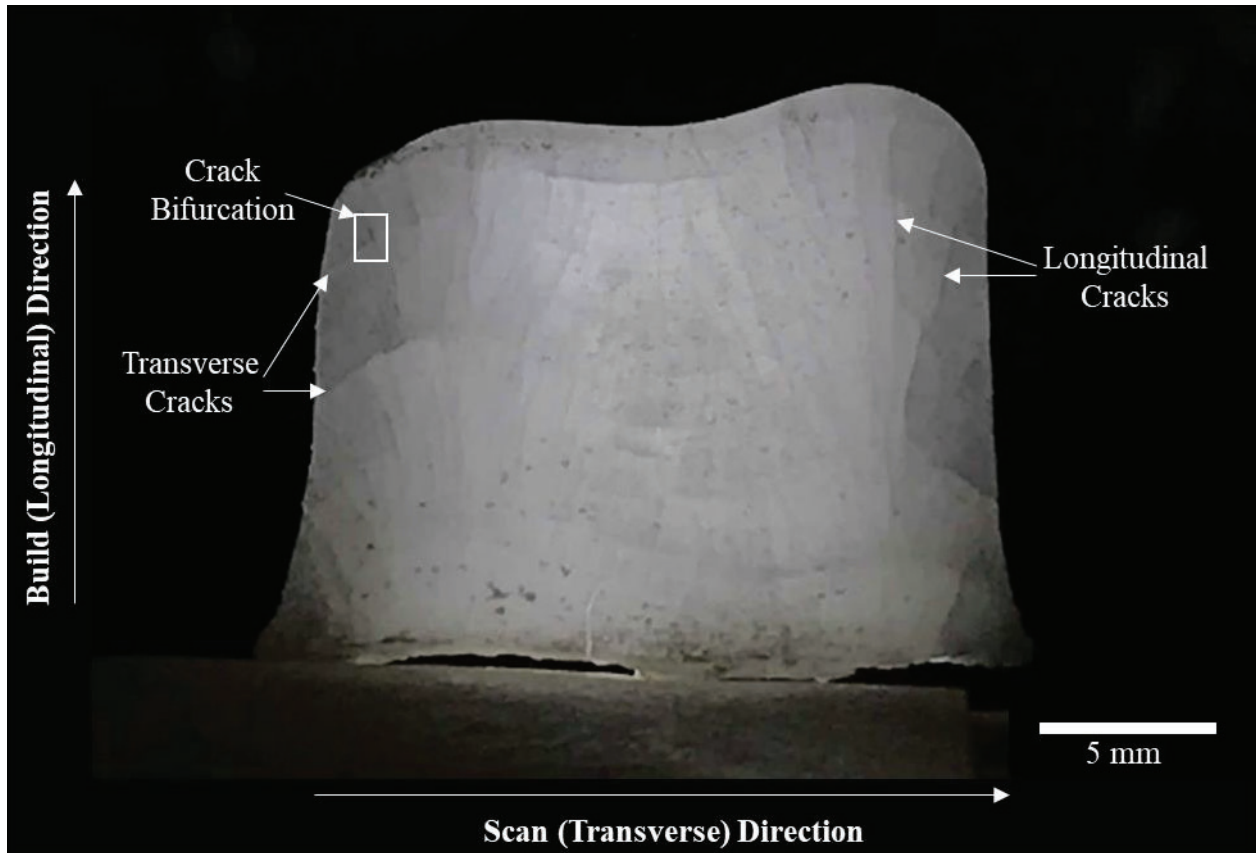


Figure 5 Side view of a MAS sample showing significant cracking in the longitudinal direction with fewer transverse cracks

Transverse cracks (along the scan direction) were observed mostly near the sides of thin wall structures, extending up to 5 mm along the scan direction. Transverse cracks initiated at defects typically located near the edges of the deposited thin wall structures. Immediately after deposition, the part of the melt pool at the interaction zone with the previous layer solidified first due to the high conduction rates through the lower layers. Volume contraction, during solidification, of the upper portion of the melt pool creates a bending moment on these layers resulting in tensile forces parallel to the build direction at the sides of thin wall structures [15]. Cracks would be formed if the tensile stresses were higher than the strength of the newly deposited

material. However, transverse crack length was typically limited due to crack bifurcation into the preferential fracture direction, i.e., along the grain boundary of columnar structures as discussed above. Further studies will be performed to investigate the effects of processing parameters on crack prevalence within the deposited MAS ceramics.

Transverse cracks were seen to be susceptible to crack bifurcation, but also crack deflection guided by residual pores. Figure 6 shows a transverse crack extending through the cross-section of a polished MAS sample. This crack was subject to crack deflection during propagation, forming a zig-zag pattern by connecting residual pores, indicating that the cracks consumed less energy by connecting pores as opposed to planar propagation. Thus, it is necessary to investigate how to lower the porosity level, which helps minimize the crack formation within the deposited ceramic samples.

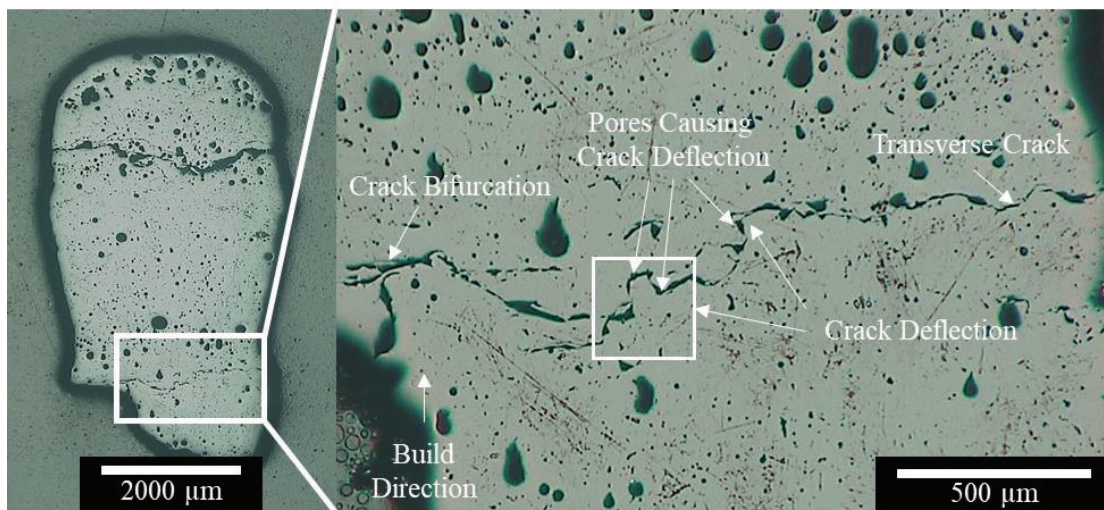


Figure 6: Cross-sectional view of MAS sample showing a transverse crack with crack deflection due to residual pores and crack bifurcation

Longitudinal cracks commonly occurred near the substrate of the printed samples as shown in Figure 7. This was mainly due to the high temperature gradient near the substrate-deposition interaction zone. The solid substrate was at a lower temperature than the deposited material, and therefore contracted considerably less during cooling processes. Thus, the substrate would undergo compression stresses while the deposition layers was under tensile stress. As a result, the tensile stresses exceeded the strength of the deposited material causing crack initiation and propagation to occur at the substrate-deposition interaction zone. The longitudinal cracks present at the substrate-deposition interface typically only extended approximately 1 mm in the build direction since the temperature differential, and therefore tensile stress, decreased with an increasing distance from the substrate.

Another consequence of the high temperature differential at the substrate-deposition interaction zone was that the deposited material experienced much more volume contraction than the substrate during cooling. The volume contraction causes a bending moment to run through the sample, and as a result, high tensile forces were present along the sides of the deposited material

near the substrate-deposition interaction zone. Occasionally, single and long cracks were observed in the deposited samples as shown in Figure 7, which were deflected by the residual pores. Tensile forces generated were also typically large enough to cause brittle failure between deposited layers and the substrate and frequently led to the delamination of the thin wall samples from the substrate. Due to the bending moment, warping of the deposited material was typically seen, especially in long thin wall structures (length >25 mm) in the preliminary tests. To minimize or even eliminate the longitudinal cracks near the substrate, as well as the delamination of the deposited part, it is suggested to preheat the substrate prior to the deposition process. Sufficient substrate preheating would significantly reduce thermal gradients in this region and thus reduce tensile stresses and bending moment in the samples.

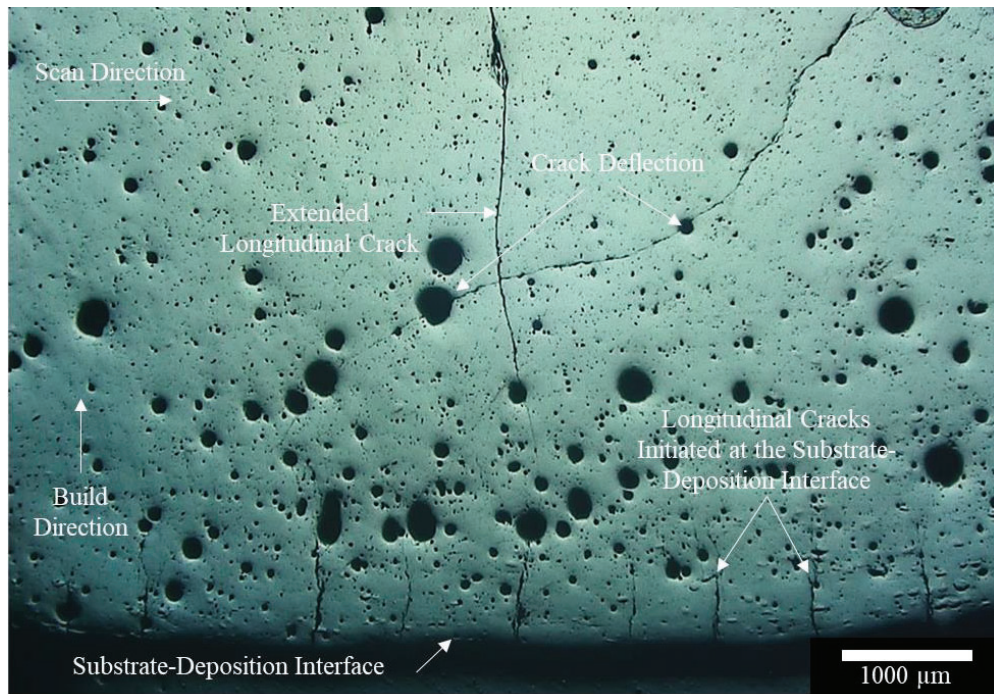


Figure 7: The optical micrograph of the polished sample side view showing severe longitudinal cracking near substrate-deposition interface due to contraction induced tensile stresses in the deposited MAS structure

3.3 Porosity Characterization of MAS Samples

3.3.1 Effects of Laser Scan Speed on Residual Porosity

The effect of scan speed on the porosity of fabricated parts was investigated and Figure 8 shows the primary results. The general trend for scan speed with respect to porosity was that as scan speed increased, there was an increase in porosity as shown in Figure 8A. The minimum porosity was 9.8% and the maximum was 14.5% at scan speeds of 1000 mm/min and 5000 mm/min, respectively. The results for the density of the entire structure can be seen in Figure 8B.

The highest average density was 96.6%, while the lowest was 92.5% at scan speeds of 4000 mm/min and 1000 mm/min, respectively. The density analysis of the entire part showed a clear trend, where increased scan speed resulted in increased relative density.

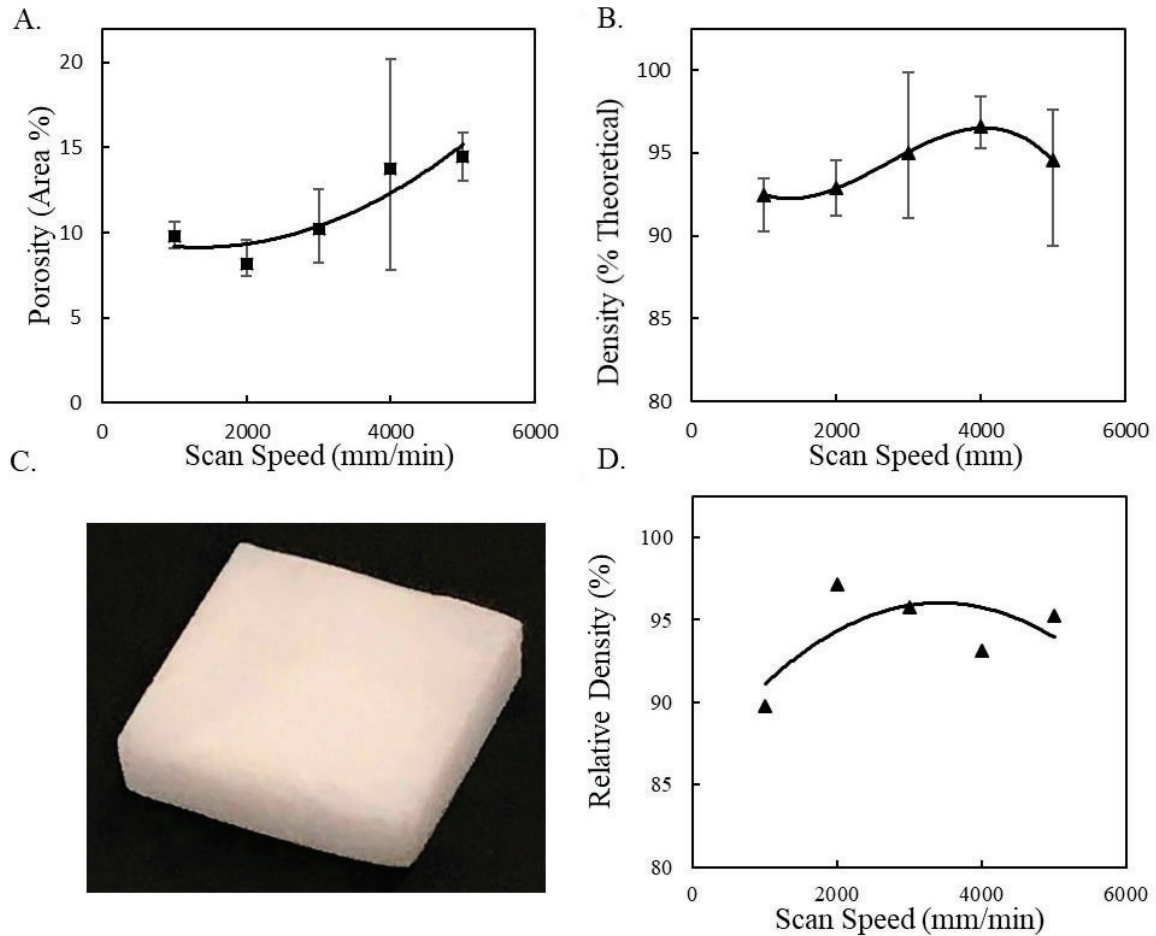


Figure 8 Results from scan study on A. Porosity area and B. Sample density, also showing C. Thin wall sample ground to cuboid shape, and D. Density measurements of the post processed samples.

It should be noted that this trend was not correlated well with the porosity results for this study. It was expected that an increase in density would be related to a reduction in porosity. It is important to note that open porosity may have significantly affected measured density of samples showing higher porosity. As the frequency of pores increased, there was a greater chance that pores would connect. Connected pores that were open to the surface would fill with distilled water used during density testing, resulting in artificially high measured densities. Samples with lower porosity levels, and hence less open porosity, would have a smaller interior volume filled with distilled water, resulting in lower but more accurate measured densities. Increased open porosity could help to explain why density increased while porosity increased. The problem with measuring the density for the entire sample was that it may not be representative of the usable central portion. Since the area used for porosity analysis only represented a portion of the entire sample, it is possible that the porosity results could vary considerably depending on where the cross-section is

taken. When fabricating parts with this method, post processing would be necessary to remove the unstable regions which typically show atypical properties and porosity levels, especially within the top and bottom layers. Therefore, samples ground to cuboid shape, shown in Figure 8C, were additionally analyzed through density measurements. To achieve the desired cuboid shape, samples were ground on all sides via a 45 micron silicon carbide grinding wheel. Since a small number of samples were prepared in this manner, samples were hand ground by pressing one side of the sample onto the rotating grinding wheel until a plane surface was achieved. This was repeated for all six sides of each sample. The density results of the post-processed parts were shown in Figure 8D. It is interesting to note that the general trend for density measurements first increased and then decreased with an increasing scan speed, which was opposite of the findings for the density of the entire samples. This indicates that the porosity levels in the unstable regions, primarily within the top most layers, significantly affected the average density for the entire sample. The general trend in the porosity analysis here was that increased scan speed results in increased porosity is similar to the results for laser engineered net shaping of 17-4PH stainless steel [32]. It was assumed that the initial powder porosity played a role in the increase observed. An explanation for this result is that increased scan speed resulted in shallower melt pool depths, and decreased amount of time for gasses contained within powder conglomerates to escape before being covered by the following layer. At higher scan speeds, decreased laser-deposited layer interaction time also produced lower melt pool temperatures and increased viscosity, thus limiting gas removal mechanisms.

3.3.3 Effects of Laser Power on Residual Porosity

At high laser powers, the porosity was shown to decrease dramatically, e.g., with porosity as low as 1.2% at a laser power of 485 W. As shown in Figure 9A, the fabricated samples at 275 W showed a wide range of pore sizes distributed throughout the cross-section. With many small pores, a significant number of medium-to-large pores were observed. On the other hand, thin wall samples produced at 485 W, seen in Figure 9B, showed only a few large pores with most pores being very small. Medium sized pores were primarily absent from the printed at 485 W.

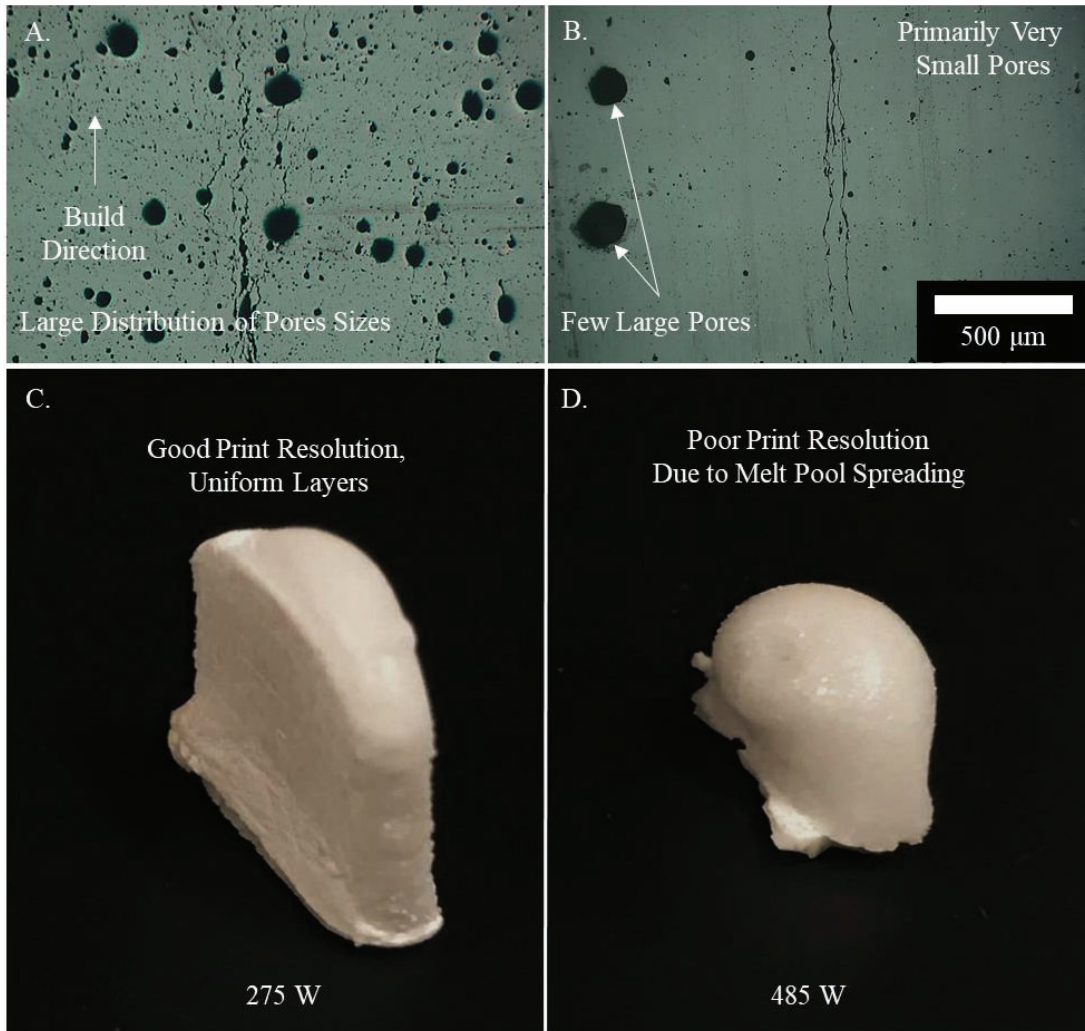


Figure 9: Results from laser power study including A. Micrograph of sample cross-section fabricated at 275 W showing a high frequency of large pores, B. Micrograph of sample cross-section produced at 485 W with greatly reduced pore size and frequency, C. Thin wall structure printed at 275 W showing good printability and uniform layers, and D. Thin wall structure exhibiting irregular shape and poor resolution due to a higher laser intensity at 485 W. Both samples were printed using 1000 mm/min scan speed and 2.1 g/min powder flow rate.

A possible explanation for this result is that a high laser power as sufficient to maintain a high enough temperature in deposited layers to allow gasses to combine and escape through the surface of the melt pool. In particular, the few trapped large pores in Figure 9B, larger than those seen in Figure 9A, indicated that the increased duration at a high temperature allowed the gasses to combine into larger pores. It should be noted that samples produced at 485 W exhibited a decreased stability of the melt pool and thus exhibited a part of an irregular shape. Figure 12C shows a thin wall structure fabricated with the laser power 275 W, which is uniform in shape along the build direction due to a relatively good print resolution. In contrast, Figure 9D demonstrates the difficulty of fabricating thin wall structures at a high laser power. The melt pool spread significantly due to decreased melt viscosity at the higher temperatures, meaning that the thin wall structure was much wider than structures produced at lower laser powers. The width of the sample

printed at 485 W was 6.3 mm, while the sample printed at 275 W was 3.8 mm wide. Hence, print resolution was reduced by nearly a factor of two by increasing laser power to 485 W. The decreased resolution seen at high laser powers would pose challenges in producing small structures with high dimensional accuracy without reducing laser spot size.

3.3.4 Translucency Demonstration

In order to examine the feasibility of the proposed deposition process in fabricating MAS samples with transparency, or at least translucency, thin wall samples were first prepared using the optimal processing parameters showing minimal porosity. The parameters used included 275 W, 1000 mm/min, and 0.8 g/min for laser power, scan speed, and powder flow rate, respectively. The sample was polished to a thickness of 0.7 mm. Figure 10 shows that a MAS sample with translucency was successfully made through laser direct deposition. The Missouri S&T logo was visible through the sample. It should be noted that thicker samples appeared to be opaque primarily due to cracking and residual porosity. Though not showing a transparent sample, this well demonstrated the viability of the proposed laser direct deposition in directly printing MAS samples. In combination with other benefits of 3D printing samples of complex geometries, this process showed great potentials in the fabrication of high strength transparent ceramics. Further studies will be performed in optimizing the processing parameters and their effects on the transparency of laser direct deposited MAS ceramics.

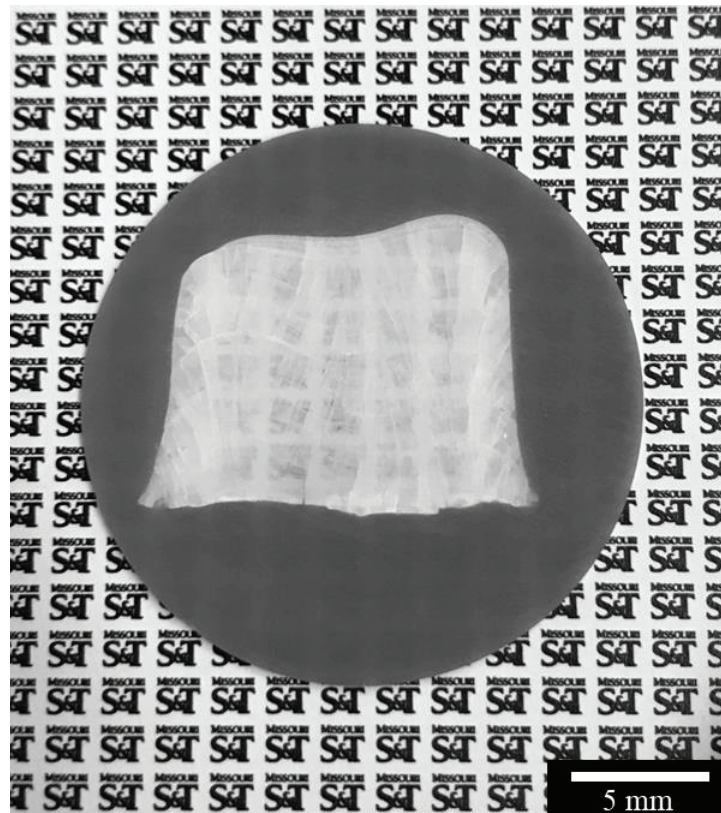


Figure 10: Polished MAS sample demonstrating translucency over a grid of Missouri S&T logos

Conclusions

This paper demonstrated the feasibility of laser direct deposition in rapidly fabricating MAS parts that would be otherwise difficult and expensive to manufacture using traditional methods. The effects of processing parameters on the microstructure of MAS ceramics fabricated by laser direct deposition was studied, with cracking and porosity being key issues in affecting the transparency of the fabricated parts. It was shown that translucent MAS ceramic samples could be successfully fabricated. The process described in this paper used precursors MgO and Al₂O₃ for direct laser synthesis, without the need for prior synthesis into MAS powders, typically a lengthy and expensive process. The typical microstructure of MAS ceramics was found to be dominated by columnar grains, orientated in the build direction but at a tilt angle toward the direction of incoming powder flow due to cooling by the powder conveying gas. Microcracks, as a significant defect of MAS ceramics by direct laser deposition, were primarily orientated in the build direction along grain boundaries. Future work will include an in-depth study on how grain size, and microcracks are affected by processing parameters including laser scan speed and powder flow rate. It was also shown that increased scan speed resulted in an increase in total porosity. Increased laser power resulted in samples with the lowest porosity levels through increased localized temperatures and longer high temperature durations. However, this reduction in porosity came at the costs of decreased resolution and dimensional accuracy. Future work includes studying the effects of processing parameters on the transparency of laser direct deposited MAS ceramics.

Acknowledgements

The authors would like to thank Dr. Jeremy Watts for helpful discussions, advice, and assistance with sample preparation for microstructural analysis. We would also like to extend a special thanks to Aditya Thakur for his assistance in capturing scanning electron micrographs of the powders used in this study.

References

- [1] G. Bonnefont, G. Fantozzi, S. Trombert, and L. Bonneau, "Fine-grained transparent MgAl₂O₄ spinel obtained by spark plasma sintering of commercially available nanopowders," *Ceram. Int.*, vol. 38, no. 1, pp. 131–140, 2012.
- [2] A. Krell, J. Klimke, and T. Hutzler, "Advanced spinel and sub- μm Al₂O₃ for transparent armour applications," *J. Eur. Ceram. Soc.*, vol. 29, no. 2, pp. 275–281, 2009.
- [3] I. Ganesh, "A review on magnesium aluminate (MgAl₂O₄) spinel: synthesis, processing and applications," *Int. Mater. Rev.*, vol. 58, no. 2, pp. 63–112, 2012.
- [4] L. Lallemand, G. Fantozzi, V. Garnier, and G. Bonnefont, "Transparent polycrystalline alumina obtained by SPS: Green bodies processing effect," *J. Eur. Ceram. Soc.*, vol. 32, no. 11, pp. 2909–2915, 2012.
- [5] A. Krell, P. Blank, and H. Ma, "Processing of High-Density Submicrometer Al₂O₃ for New Applications," *J. Am. Ceram. Soc.*, vol. 86, pp. 546–553, 2003.
- [6] F. Yan, W. Xiong, and E. J. Faierson, "Grain structure control of additively manufactured metallic materials," *Materials (Basel)*, vol. 10, no. 11, p. 1260, 2017.
- [7] D. Baillis, L. Pilon, H. Randrianalisoa, R. Gomez, and R. Viskanta, "Measurements of radiation characteristics of fused quartz containing bubbles," *J. Opt. Soc. Am. A*, vol. 21,

- no. 1, p. 149, 2004.
- [8] L. Pilon and R. Viskanta, "Radiation characteristics of glass containing gas bubbles," *J. Am. Ceram. Soc.*, vol. 86, no. 8, pp. 1313–1320, 2003.
 - [9] Z. Liu, M. Jia, X. Liu, Q. Jing, and P. Liu, "Fabrication and microstructure characterizations of transparent polycrystalline fluorite ceramics," *Mater. Lett.*, vol. 227, pp. 233–235, 2018.
 - [10] Q. Li, G. P. Zhang, H. Wang, and L. W. Lei, "Effect of pores on transmission properties of transparent ceramics," *Optoelectron. Adv. Mater. Rapid Commun.*, vol. 5, no. 6, pp. 673–676, 2011.
 - [11] A. Krell and A. Bales, "Grain size-Dependent hardness of transparent magnesium aluminate spinel," *Int. J. Appl. Ceram. Technol.*, vol. 8, no. 5, pp. 1108–1114, 2011.
 - [12] R. M. Mahamood, E. T. Akinlabi, M. Shukla, and S. Pityana, "Characterizing the Effect of Processing Parameters on the Porosity of Laser Deposited Titanium Alloy Powder," *J. Manuf. Sci. Eng.*, vol. 2, no. December 2013, pp. 904–908, 2014.
 - [13] F. Ning, Y. Hu, Z. Liu, W. Cong, Y. Li, and X. Wang, "Ultrasonic Vibration-Assisted Laser Engineered Net Shaping of Inconel 718 Parts: A Feasibility Study," *Procedia Manuf.*, vol. 10, pp. 771–778, 2017.
 - [14] F. Niu, D. Wu, S. Yuan, G. Ma, and Z. Jia, "Title Effect of layer thickness on crack suppression in laser engineered net shaping of ceramic structure," in *Proceedings of the 3rd International Conference on Progress in Additive Manufacturing (Pro-AM 2018)*, 2018, pp. 464–469.
 - [15] F. Y. Niu, D. J. Wu, S. Yan, G. Y. Ma, and B. Zhang, "Process Optimization for Suppressing Cracks in Laser Engineered Net Shaping of Al₂O₃ Ceramics," *Jom*, vol. 69, no. 3, pp. 557–562, 2017.
 - [16] Y. Hu, F. Ning, W. Cong, Y. Li, X. Wang, and H. Wang, "Ultrasonic vibration-assisted laser engineering net shaping of ZrO₂-Al₂O₃ bulk parts: Effects on crack suppression, microstructure, and mechanical properties," *Ceram. Int.*, vol. 44, no. 3, pp. 2752–2760, 2018.
 - [17] V. K. Balla, S. Bose, and A. Bandyopadhyay, "Processing of bulk alumina ceramics using laser engineered net shaping," *Int. J. Appl. Ceram. Technol.*, vol. 5, no. 3, pp. 234–242, 2008.
 - [18] F. Niu, D. Wu, F. Lu, G. Liu, G. Ma, and Z. Jia, "Microstructure and macro properties of Al₂O₃ ceramics prepared by laser engineered net shaping," *Ceram. Int.*, vol. 44, no. 12, pp. 14303–14310, 2018.
 - [19] W. Konrad, "Net Shaped High Performance Oxide Ceramic Parts by Selective Laser Melting," vol. 5, no. 2, pp. 587–594, 2010.
 - [20] Z. Fan, M. Lu, and H. Huang, "Selective laser melting of alumina : A single track study," *Ceram. Int.*, vol. 44, no. 8, pp. 9484–9493, 2018.
 - [21] J. Wilkes, Y. C. Hagedorn, W. Meiners, and K. Wissenbach, "Additive manufacturing of ZrO₂-Al₂O₃ ceramic components by selective laser melting," *Rapid Prototyp. J.*, vol. 19, no. 1, pp. 51–57, 2013.
 - [22] Y. Zheng, K. Zhang, T. T. Liu, W. H. Liao, C. D. Zhang, and H. Shao, "Cracks of alumina ceramics by selective laser melting," *Ceram. Int.*, vol. 45, no. 1, pp. 175–184, 2019.
 - [23] F. Niu, D. Wu, S. Zhou, and G. Ma, "Power prediction for laser engineered net shaping of Al₂O₃ ceramic parts," *J. Eur. Ceram. Soc.*, vol. 34, no. 15, pp. 3811–3817, 2014.
 - [24] D. Wu, J. Wang, G. Ma, Z. Jin, F. Niu, and J. Zhuang, "Rapid Fabrication of Eutectic Ceramic Structures by Laser Engineered Net Shaping," *Procedia CIRP*, vol. 42, no. Isem

- Xviii, pp. 91–95, 2016.
- [25] K. C. Datsiou, E. Saleh, F. Spirrett, R. Goodridge, I. Ashcroft, and D. Eustice, “Additive manufacturing of glass with laser powder bed fusion,” *J. Am. Ceram. Soc.*, no. February, pp. 4410–4414, 2019.
 - [26] J. Luo, L. J. Gilbert, C. Qu, R. G. Landers, D. A. Bristow, and E. C. Kinzel, “Additive Manufacturing of Transparent Soda-Lime Glass Using a Filament-Fed Process,” *J. Manuf. Sci. Eng.*, vol. 139, no. 6, p. 061006, 2016.
 - [27] L. Kumari, W. Z. Li, C. H. Vannoy, R. M. Leblanc, and D. Z. Wang, “Synthesis, characterization and optical properties of Mg(OH)₂ micro-/nanostructure and its conversion to MgO,” *Ceram. Int.*, vol. 35, no. 8, pp. 3355–3364, 2009.
 - [28] J. C. Yu, A. Xu, L. Zhang, R. Song, and L. Wu, “Synthesis and Characterization of Porous Magnesium Hydroxide and Oxide Nanoplates,” *J. Phys. Chem. B*, vol. 108, no. 1, pp. 64–70, 2004.
 - [29] S. Preibisch, S. Saalfeld, and P. Tomancak, “Globally optimal stitching of tiled 3D microscopic image acquisitions,” *Bioinformatics*, vol. 25, no. 11, pp. 1463–1465, 2009.
 - [30] U. Ta, V. Carle, U. Scha, and M. J. Hoffmann, “Preparation and Microstructural Analysis of High-Performance Ceramics,” *Metallogr. Microstruct.*, vol. 9, pp. 1057–1066, 2018.
 - [31] C. Aksel, B. Rand, F. L. Riley, and P. D. Warren, “Thermal shock behaviour of magnesia-spinel composites,” *J. Eur. Ceram. Soc.*, vol. 24, no. 9, pp. 2839–2845, 2004.
 - [32] D. F. Susan, J. D. Puskar, J. A. Brooks, and C. V. Robino, “Quantitative characterization of porosity in stainless steel LENS powders and deposits,” *Mater. Charact.*, vol. 57, no. 1, pp. 36–43, 2006.
 - [33] J. Choi and Y. Chang, “Characteristics of laser aided direct metal/material deposition process for tool steel,” *Int. J. Mach. Tools Manuf.*, vol. 45, no. 4–5, pp. 597–607, 2005.